PHYSICAL REVIEW B VOLUME 38, NUMBER 5 15 AUGUST 1988-I

Optical dielectric function of high-stage potassium graphite intercalation compounds: Experiment and theory

M. H. Yang and P. C. Eklund

Department of Physics and Astronomy, University of Kentucky, Lexington, Kentucky 40506

(Received 14 September 1987; revised manuscript received 14 March 1988)

Optical reflectance of the stage-2–4 graphite potassium intercalation compounds in the range 0.2–6 eV has been measured and the experimental dielectric functions have been derived from Kramers-Kronig analyses. The parameters of a two-dimensional tight-binding model Hamiltonian are obtained by comparison of the calculated interband dielectric function with the experimental data. Good agreement between experiment and the model is obtained. Narrow peaks associated with low-energy interband transitions between graphitic π^* conduction bands observed in the third- and fourth-stage compounds are found to occur at photon energies approximately equal to the difference in electrostatic potential energy between bounding and interior carbon layers. A simple k dependence of the nearest-neighbor carbon transfer integral parameter γ_0 is introduced to the model Hamiltonian to obtain quantitative agreement with ~ 4.6 eV interband spectral feature associated with the M points in a graphitic hexagonal Brillouin zone. The c-axis charge distribution, density of states at the Fermi level, and the extremal Fermi cross-sectional areas are also calculated and compared with values obtained from NMR, specific-heat, and de Haas–van Alphen experiments.

I. INTRODUCTION

Graphite intercalation compounds (GIC's), as a class of quasi-two-dimensional metals, have been studied extensively over the past ten years.[1,2] The intercalation of layers into the graphitic host is accompanied by a transfer of electrons between intercalate and carbon layers. Depending on whether the graphite layers in the GIC acquire positive or negative charge, the GIC's are classified as acceptor type (+) or donor type (−). One of the most striking properties of GIC's of either type is the formation of the c-axis superlattice due to the periodic insertion of intercalate layers. An experimental measure of the distribution of net layer charge in GIC's is essential to a quantitative understanding of the stage-dependent optical and electronic properties of these materials as well as the very formation of the c-axis superlattice itself. Several theoretical calculations[3–10] have indicated that in the third- and higher- ($n \geq 3$) stage GIC's, where the stage index n refers to the number of carbon layers between periodically inserted intercalate layers, the carbon layers next to the intercalate layers (termed "bounding" carbon layers) will acquire most of the charge transferred from the intercalate layers. The other carbon layer(s) are referred to as interior carbon layers. The difference in net layer charge is, of course, related to their average layer electrostatic potential. One therefore expects carbon π bands primarily associated with interior carbon layers to be raised in energy with respect to those primarily associated with bounding carbon layers.

Despite numerous recent optical studies on various GIC's over the past ten years,[1,11,12] no previous optical study has attempted to study quantitatively the distribution of c-axis charge. Comparisons between optical data and theoretical calculations for $n \geq 3$ compounds have appeared,[13,14] and have been mostly at the qualitative or semiquantitative level. Calculations of the dielectric function $\epsilon(\omega)=\epsilon_1(\omega)+i\epsilon_2(\omega)$ (Refs. 13–15) have been published only for low-stage GIC's ($n=1,2$), where the net layer charge on all carbon layers is thought to be the same, or nearly the same.

The intent of this paper is to present experimental results of the stage-dependent dielectric function of the stage-$n=2$–4 prototypical donor GIC's KC_{12n} and quantitatively compare the results to band theory. To the best of our knowledge, we present the first calculation of the dielectric response for higher-stage donor-type GIC's. Blinowski and Rigaux[5] reported the relative optical transition probabilities between bonding carbon (π) and antibonding carbon (π^*) bands near the K point for a stage-3 acceptor compound, but they assumed equal net charge on the interior and bounding carbon layers. Hawrylak has also calculated the in-plane dielectric response for a stage-3 $SbCl_5$-GIC using a self-consistent tight-binding band model.[6]

Our bands are calculated using the phenomenological, two-dimensional (2D) tight-binding model of Saito and Kamimura.[10] To achieve good agreement between the optical data and theory we have had to adjust the values of some of the parameters in the model of Saito and Kamimura, as well as introduce a simple k dependence in the nearest-neighbor in-plane carbon-carbon transfer integral γ_0.

The paper is arranged as follows. In Secs. II and III we describe, respectively, the experimental details and Kramers-Kronig transformations. In Sec. IV we give a detailed account of the model Hamiltonian and our procedures for the calculations. In Sec. V we discuss the band structure and its relation to the optical, de Haas–van Alphen, specific-heat, and nuclear magnetic resonance (NMR) data.

II. EXPERIMENTAL PROCEDURE

Stage-2–4 potassium graphite intercalation compounds were prepared in Pyrex glass ampoules by the conventional two-temperature method.[16] Highly oriented pyrolytic graphite (HOPG) and potassium metal (99.9% pure) are used as initial reagents. HOPG plates ($5\times5\times0.2$ mm^3) were kept at higher temperatures than the potassium in the reaction ampoule to avoid condensation of the K onto the sample surfaces. The stage index n of the final compounds depended on the temperature difference ΔT between the HOPG and K, and n increases as ΔT increases. In the present work, the potassium was kept at a constant temperature $T_K=250\,^\circ\mathrm{C}$. Stage 2–4 K GIC's were obtained, respectively, after two days at the following ΔT: 100, 150, and 200 °C. The temperature of both potassium and graphite were monitored by two separate thermocouples attached to the respective ends of the glass ampoule.

Well-staged samples were characterized by $(00l)$ x-ray diffraction as a deep bulk probe, and by Raman scattering as a probe of the stage index in the optical skin depth.[1,2] The $(00l)$ x-ray data[1,16,17] and Raman-scattering data from the graphitic ~1600-cm^{-1} modes[18] were found to be in good agreement with the literature. After characterization, the samples were transferred in a high-purity He glove box with $P_{\mathrm{H_2O}},P_{\mathrm{O_2}}\leq1$ ppm into an optical cell with a KBr window. The optical cell was subsequently evacuated to a pressure of 10^{-6} Torr which was maintained by a small $[\frac{3}{4}$-(l/s)$]$ ion pump. Careful sample transfer and use of the evacuated optical cell was essential to obtaining reproducible results. The near-normal-incidence reflectance data were collected in the range 0.2–6 eV for stage 2–4 K GIC's using a Perkin-Elmer prism monochromator (model No. 83, with $\mathrm{CaF_2}$ and $\mathrm{SiO_2}$ prisms). The spectra were obtained by comparing the reflectance of incident light from the sample to that from a standard reference mirror $\mathrm{Al(MgF_2)}$. The absolute reflectance was then obtained by correcting for the loss of light due to the KBr window. The correction is important only above 4 eV. Reflectance spectra of $\mathrm{KC_{36}}$ and $\mathrm{KC_{48}}$ that we published previously[12] were not corrected for absorption in the KBr window in the ultraviolet, and this correction (made herein) raises the reflectance somewhat in the range 4–6 eV. Further details of our optical technique and apparatus are available in Refs. 12 and 19.

III. EXPERIMENTAL RESULTS

In Fig. 1 we present the reflectance spectra (dots) of the stage-2–4 K GIC's in the energy range 0–6 eV. Each spectrum exhibits a rapid decline in reflectance $R(\omega)$ in the region 1–2 eV, characteristic of a metallic plasma. The position of this rapid decline, or "Drude edge," down-shifts from 1.6 eV for $\mathrm{KC_{24}}$ to 1.2 eV for $\mathrm{KC_{36}}$ to 1.0 eV for $\mathrm{KC_{48}}$. These shifts are consistent with a decrease of the free-electron density with increasing stage index. For $\mathrm{KC_{36}}$ and $\mathrm{KC_{48}}$, we observe narrow low-energy inter-π^*-band absorption structure 0.6–0.7 eV, similar to the reported inter-valence-band absorption in acceptor-type GIC's.[15,19,20] Our observation confirms earlier reports[21] of low-energy structure in the differential reflectance spectra of high-stage K-GIC's, though at that time the nature of the interband structure, or its stage dependence, were not clearly understood. Above the Drude edge, the reflectance in Fig. 1 rises with increasing ω due to the onset of π (valence)$\rightarrow\pi^*$ (conduction) interband absorption. By analogy with pristine graphite, the broad peak at ~4.6 eV in each spectrum is associated with $\pi\rightarrow\pi^*$ transitions near the M points in a graphitic Brillouin zone.[12,22] The solid line in each figure represents the calculated reflectance (discussed below) due to free-carrier and low-energy ($E<1$ eV) $\pi^*\rightarrow\pi^*$ interband transitions. The misfit between the solid line and the experimental reflectance in Fig. 1 near the bottom of the plasma edge is due to higher-energy $\pi\rightarrow\pi^*$ interband absorption not included in the calculation.

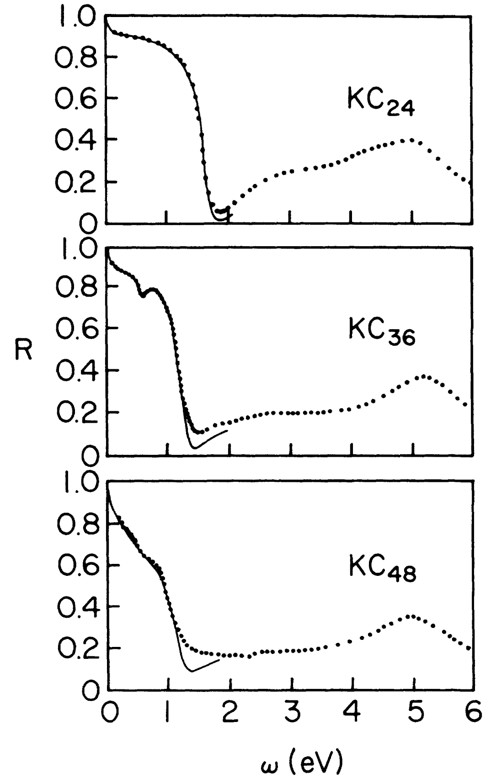

FIG. 1. Reflectance spectra of stage-2–4 K GIC's. The solid lines are calculated from Eq. (1).

To separate interband and intraband (or free-carrier) contributions to the dielectric function, we fit both the low-energy experimental reflectance $R(\omega)$ and the dielectric function $\epsilon(\omega)$,[23]

$$\epsilon(\omega)=\epsilon_\infty-\frac{\omega_p^2}{\omega(\omega+i/\tau_D)}+\sum_j\frac{-f_j}{\omega^2-\omega_j^2+i\omega\Gamma_j}\,, \qquad (1)$$

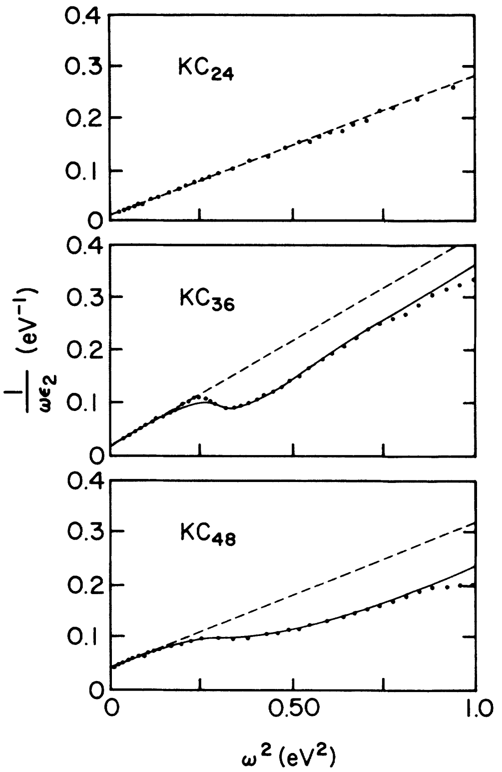

FIG. 2. $1/\omega\epsilon_2$ vs ω^2 for stage-2–4 K GIC's. The dots are the experimental data; the dashed and solid lines correspond, respectively, to the free carrier and to the free-carrier plus interband contributions given by Eq. (1).

where ϵ_∞ is the core dielectric constant, the second term is the free-electron or Drude contribution parametrized by an effective plasma frequency ω_p and mean carrier lifetime τ_D, while the third term is the interband contribution described by a sum of Lorentz oscillators parametrized by the strength f_j, center frequency ω_j, and width Γ_j. The 0.6-eV oscillators are included in the low-energy data analysis to obtain a reliable value for ω_p.

In order to carry out a Kramers-Kronig (KK) analysis of $R(\omega)$ to yield the dielectric function, the reflectance data were first extended to lower energy by Eq. (1), where $R(\omega)$ is calculated according to $R(\omega)=|(\sqrt{\epsilon}-1)/(\sqrt{\epsilon}+1)|^2$. The high-energy extensions of $R(\omega)$ were based on the reflectance of density-scaled graphite, since KC_{24n} is mostly graphitic carbon. A detailed discussion of the data extensions and KK analysis are available in Ref. 12. The zero crossing of $\epsilon_1(\omega)$ for each compound is known as the screened plasma frequency ω_p^* of the graphitic π^* conduction electrons and corresponds approximately to the position of the Drude edge. Values for ω_p^* are found to be 1.59 eV for KC_{24}, 1.33 eV for KC_{36}, and 1.18 eV for KC_{48}.

In Fig. 2 we plot $1/\omega\epsilon_2$ versus ω^2 to display the low-energy Drude behavior of the stage-2–4 compounds. The dots are experimental data, the dashed lines represent the calculated free-carrier contribution, and the solid lines in the KC_{36} and KC_{48} panels represent the sum of the free-carrier and low-energy interband contributions calculated from Eq. (1). In this plot, linear behavior indicates a free-carrier contribution well described by the Drude approximation, where the slope and intercept yield the unscreened plasma frequency ω_p and the relaxation time τ_D. The departure of the data from linear behavior indicates the onset of interband absorption. The interband oscillator and Drude parameters used to calculate the curves in Figs. 1 and 2 appear in Table I. These parameters should be viewed as a final self-consistent set used to extend $R(\omega)$ to lower energy, as well as to fit $R(\omega)$ and $1/\omega\epsilon_2$. The results of Fig. 2 show that, for stages 3 and 4, the interband contribution to ϵ_2 persists down to energies $\omega \sim (0.25\ \text{eV}^2)^{1/2}$. Furthermore, for the case of stage 2, a Drude contribution provides a very satisfactory description of the ϵ_2 data below $\omega \sim 1.0$ eV; that is, we see no evidence for a low-energy interband absorption in stage 2.

IV. THEORY

The stage-dependent Hamiltonians used in our calculation are based on 2D tight-binding model of Saito and Kamimura.[10] Their band parameters[10] were determined by the method of least squares to match as closely as possible the self-consistent results of Ohno and Kamimura,[9] which were calculated in accordance with the following assumptions: (1) hybridization between graphite and intercalant orbitals are negligible; (2) no charge flow occurs between graphite layers separated by an intercalate layer,

TABLE I. Experimental values for c-axis repeat distance (I_c), Drude, and $\pi^* \rightarrow \pi^*$ interband oscillator parameters. For definitions of the symbols see text.

		Drude parameters			Interband oscillator parameters					
Stage	I_c (Å)	ω_p (ω_p^*) (eV)	$\omega_p\tau_D$	ϵ_∞	ω_1 (eV)	Γ_1 (eV)	f_1 (eV^2)	ω_2 (eV)	Γ_2 (eV)	f_2 (eV^2)
2	8.73	4.2 (1.6)	22	7.0						
3	12.10	3.4 (1.3)	15	8.0	0.57	0.075	0.16	0.63	0.22	0.7
4	15.45	3.0 (1.2)	8	8.0	0.6	0.15	0.2	0.73	0.4	1.0

and (3) ionized intercalate layers are treated as uniformly charged sheets. The tight-binding Bloch functions are constructed from $2p_z$ carbon orbitals ϕ_{2p_z} according to

$$\phi_{j\alpha}^{\mathbf{k}}(\mathbf{r})=N^{-1/2}\sum_{m} e^{i\mathbf{k}\cdot\mathbf{R}_{j\alpha}^{m}}\phi_{2p_z}(\mathbf{r}-\mathbf{R}_{j\alpha}^{m}) , \tag{2}$$

where j denotes the jth graphite layer, α represents the particular carbon site, and the summation on m is over all equivalent carbon sites in the jth layer. The Hamiltonians constructed from these Bloch functions are given, for stage 2, by[10]

$$H(\mathbf{k})=\begin{bmatrix} \delta_1 & \gamma_0 h(\mathbf{k}) & \gamma_1 & \gamma_4 h^*(\mathbf{k}) \\ \gamma_0 h^*(\mathbf{k}) & -\delta_1 & \gamma_4 h^*(\mathbf{k}) & \gamma_3 h(\mathbf{k}) \\ \gamma_1 & \gamma_4 h(\mathbf{k}) & \delta_1 & \gamma_0 h^*(\mathbf{k}) \\ \gamma_4 h(\mathbf{k}) & \gamma_3 h^*(\mathbf{k}) & \gamma_0 h(\mathbf{k}) & -\delta_1 \end{bmatrix} , \tag{3a}$$

for stage 3 by

$$H(\mathbf{k})=\begin{bmatrix} -\delta+\delta_1 & \gamma_0 h(\mathbf{k}) & \gamma_1 & \gamma_4 h^*(\mathbf{k}) & 0 & 0 \\ \gamma_0 h^*(\mathbf{k}) & -\delta-\delta_1 & \gamma_4 h^*(\mathbf{k}) & \gamma_3 h(\mathbf{k}) & 0 & 0 \\ \gamma_1 & \gamma_4 h(\mathbf{k}) & \delta+\delta_2 & \gamma_0 h^*(\mathbf{k}) & \gamma_1 & \gamma_4 h(\mathbf{k}) \\ \gamma_4 h(\mathbf{k}) & \gamma_3 h^*(\mathbf{k}) & \gamma_0 h(\mathbf{k}) & \delta-\delta_2 & \gamma_4 h(\mathbf{k}) & \gamma_3 h^*(\mathbf{k}) \\ 0 & 0 & \gamma_1 & \gamma_4 h^*(\mathbf{k}) & -\delta+\delta_1 & h(\mathbf{k}) \\ 0 & 0 & \gamma_4 h^*(\mathbf{k}) & \gamma_3(\mathbf{k}) & \gamma_0 h^*(\mathbf{k}) & -\delta-\delta_1 \end{bmatrix} , \tag{3b}$$

and for stage 4 by

$$H(\mathbf{k})=\begin{bmatrix} -\delta+\delta_1 & \gamma_0 h(\mathbf{k}) & \gamma_1 & \gamma_4 h^*(\mathbf{k}) & 0 & 0 & 0 & 0 \\ \gamma_0 h^*(\mathbf{k}) & -\delta-\delta_1 & \gamma_4 h^*(\mathbf{k}) & \gamma_3 h(\mathbf{k}) & 0 & 0 & 0 & 0 \\ \gamma_1 & \gamma_4 h(\mathbf{k}) & \delta+\delta_2 & \gamma_0 h^*(\mathbf{k}) & \gamma_1 & \gamma_4 h(\mathbf{k}) & 0 & 0 \\ \gamma_4 h(\mathbf{k}) & \gamma_3 h^*(\mathbf{k}) & \gamma_0 h(\mathbf{k}) & \delta-\delta_2 & \gamma_4 h(\mathbf{k}) & \gamma_3 h^*(\mathbf{k}) & 0 & 0 \\ 0 & 0 & \gamma_1 & \gamma_4 h^*(\mathbf{k}) & \delta-\delta_2 & \gamma_0 h(\mathbf{k}) & \gamma_1 & \gamma_4 h^*(\mathbf{k}) \\ 0 & 0 & \gamma_4 h^*(\mathbf{k}) & \gamma_3 h(\mathbf{k}) & \gamma_0 h^*(\mathbf{k}) & \delta-\delta_2 & \gamma_4 h^*(\mathbf{k}) & \gamma_3 h(\mathbf{k}) \\ 0 & 0 & 0 & 0 & \gamma_1 & \gamma_4 h(\mathbf{k}) & -\delta+\delta_1 & \gamma_0 h^*(\mathbf{k}) \\ 0 & 0 & 0 & 0 & \gamma_4 h(\mathbf{k}) & \gamma_3 h^*(\mathbf{k}) & \gamma_0 h(\mathbf{k}) & -\delta-\delta_1 \end{bmatrix} , \tag{3c}$$

where $h(\mathbf{k})=-\sum_s e^{i\mathbf{k}\cdot\boldsymbol{\tau}_s}$ is the basal-plane carbon structure factor,[15] and the τ_s ($s=1-3$) are the unit vectors shown in Fig. 3(a). The in-plane unit cell is shown as the dashed line. In Fig. 3(b) we show the two-dimensional graphitic Brillouin zone appropriate to the model. The γ_i's in Eqs. (3a)–(3c) are the transfer integrals between neighboring carbon sites, and δ and δ_j are linear combinations of self-energy integrals from different carbon sites (Fig. 4).[24]

In our calculation, the values of most of the band parameters remain the same as those determined by Saito and Kamimura.[10] However, we have reduced the value of the electrostatic energy parameter δ in Eqs. (3b) and (3c) for stage 3 and stage 4 from 0.46 to 0.3 eV in order to fit the position of the observed interband structure near 0.6 eV. In addition, we also have found that a k-dependent γ_0 (nearest-neighbor, in-plane transfer in-

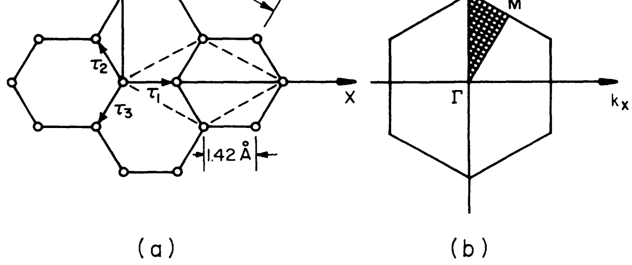

FIG. 3. Carbon-atom organization in a graphitic layer of a GIC. The dashed line in (a) indicates the unit cell. The corresponding graphitic two-dimensional Brillouin zone is shown in (b), where the shaded area represents the irreducible portion.

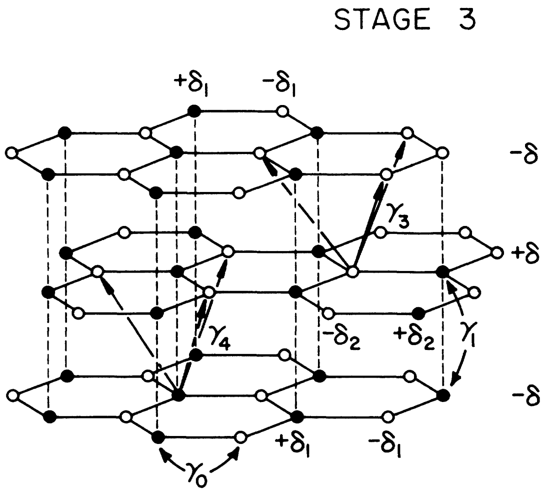

FIG. 4. Schematic view of the π-band parameters, γ's and δ's, indicating the particular carbon-atom sites involved in the stage-3 model.

tegral) is necessary to fit the position of strong broad peaks near 4.6 eV. The need for a k-dependent γ_0 reflects the fact that more distant transfer integrals (omitted from the model of Saito and Kamimura) make significant contributions to the band structure at points far removed from the K point(s). In pristine graphite, Johnson and Dresselhaus[22] have shown earlier that these distant interactions result in effective values for γ_0 of 3.2 eV at the K point(s) and 2.3 eV at the M point(s) in the Brillouin zone [Fig. 3(b)]. Furthermore, they have pointed out that the optical transition energy $\hbar\omega$ in graphite near the M point (4.6 eV) is approximately twice the effective value of γ_0 at the M point. Consistent with their observations we replace the constant γ_0 in Eqs. (3a)–(3c) with a k-dependent γ_0 given by[25]

$$\gamma_0(\kappa)=\frac{\gamma_0(0)}{1+\chi(\kappa/\kappa')} , \tag{4}$$

where κ is the length of the basal-plane wave vector measured relative to the K point and κ' is the length of the wave vector between the Γ and K points. The value of γ_0 at the K point is chosen to be 3.0 eV, consistent with previous optical work in GIC's.[15,19,20] A *stage-independent* constant χ is chosen so that $2\gamma_0=4.6$ eV at the M point, which yields a peak at this energy in the calculated $\epsilon_{\text{inter}}(\omega)$, in good agreement with the data. In Table II, we list our values for the band parameters. Parameter values used by Saito and Kamimura,[10] which are different from the present work, are also indicated in parentheses.

The graphitic π- and π^*-band $E_j(\mathbf{k})$ and wave functions $\psi_j(\mathbf{k})$ were obtained by diagonalizing the respective Hamiltonians $H(\mathbf{k})$ in Eqs. (3a) and (3b) and the density-of-states (DOS) function $D(E)$ was calculated by the standard procedure[26] of integration over the full irreducible portion of the Brillouin zone [shown as the shaded area in Fig. 3(b)]. It is given by

$$D(E)=\frac{12}{2\pi^2 I_c}\sum_j \int d^2k\, \delta(E-E_j(\mathbf{k})) , \tag{5}$$

where $E_j(\mathbf{k})$ represents the jth π band and I_c is the c-axis repeat distance. The integral was evaluated by dividing the shaded area into 10^4 uniformly distributed points; the resolution was $\Delta E=0.02$ eV. The Fermi energy E_F was then calculated by filling the available states from the bottom of the π bands up to the Fermi level[27] according to

$$N_e=\int_{-\infty}^{E_F} D(E)dE , \tag{6}$$

where N_e, the electron density in the valence (π) *and* conduction (π^*) bands for the KC_{12n} compound, is equal to one electron per C atom in the π band(s) and $1/12n$ electron per C atom in the π^* band(s). This assumes complete charge transfer from the K 4s states to the carbon π^* bands.[9,10]

We have evaluated the interband dielectric function $\epsilon_2(\omega)$ for the stage-2–4 K GIC's in the relaxation-time approximation. This method also has been used previously by Johnson and Dresselhaus[22] for pristine graphite. In this approximation, a frequency-independent value for τ is used to represent the average photoexcited electron lifetime. The in-plane dielectric function is then given by[22]

TABLE II. Present results for graphitic π and π^* tight-binding band parameters. Values in parentheses refer to those values in Ref. 10 which differ from present work. The parameters are defined in the text and in Fig. 4.

Stage	γ_0 (eV)	γ_1 (eV)	γ_3 (eV)	γ_4 (eV)	δ (eV)	δ_1 (eV)	δ_2 (eV)	χ
2	3.0 (3.3)[a]	0.32	0.21	0.21		0.0		0.7 (0)[a]
3	3.0 (3.3)[a]	0.32	0.21	0.21	0.3 (0.46)[a]	−0.018	0.011	0.7 (0)[a]
4	3.0 (3.3)[a]	0.32	0.21	0.21	0.3 (0.46)[a]	−0.018	0.011	0.7 (0)[a]

[a] From Ref. 10.

$$\epsilon_{\mu\nu}(\omega) = -\frac{e^2}{\pi^2}\frac{1}{\bar{\omega}}\sum_{i,j}{}' \frac{2\pi}{I_c}\int_{\mathrm{BZ}} \frac{d^2k}{\hbar\omega_{ij}(\mathbf{k})}\left[\frac{V_{ij}^{\mu}(\mathbf{k})V_{ji}^{\mu}(\mathbf{k})}{-\bar{\omega}+\omega_{ij}(\mathbf{k})}\right]\left[\frac{V_{j}^{\nu}(\mathbf{k})V_{ji}^{\mu}(\mathbf{k})}{-\bar{\omega}+\omega_{j}(\mathbf{k})}\right]\{f(E_j)[1-f(E_i)]\}\ , \tag{7}$$

where μ,ν refer to Cartesian coordinates in the basal plane, $\bar{\omega}=\omega+i/\tau$, and $\hbar\omega_{ij}(\mathbf{k})$ is the energy difference $E_i(\mathbf{k})-E_j(\mathbf{k})$. Equation (7) does not include indirect transitions or many-body effects. The matrix elements have been reduced to velocity matrix elements V_{ij} which are found from the gradient of the Hamiltonian $H(\mathbf{k})$,[22]

$$V_{ij} = \{U(\mathbf{k})[\nabla_k H(\mathbf{k})]U^{-1}(\mathbf{k})\}_{ij}\ , \tag{8}$$

where $U(\mathbf{k})$ is the unitary transformation that diagonalizes the Hamiltonian $H(\mathbf{k})$. We evaluated the k-space integral [Eq. (7)] over the full irreducible 2D Brillouin zone (BZ) with the same point density as that used in the DOS calculation. The Fermi-Dirac distribution was included in Eq. (7) to account for the experimental temperature (300 K). For comparison with experiment, the in-plane dielectric function was calculated according to

$$\epsilon(\omega) = \tfrac{1}{2}[\epsilon_{xx}(\omega)+\epsilon_{yy}(\omega)]\ . \tag{9}$$

V. DISCUSSION

A. Band structure

The energy band structure we calculated for stage-2, -3, and -4 K GIC's along the high-symmetry axes Γ-*K*-*M* are shown in Figs. 5(a)–5(c). The overall dispersion of these bands is quite similar to those of Saito and Kamimura.[10] For a stage-*n* compound, there are *n* conduction and *n* valence bands. All the π^* conduction bands are partially filled with electrons. For our values of the band parameters (Table II), the Fermi level is located at 1.28, 0.92, and 0.88 eV, respectively, for the stage-2, -3, and -4 K GIC's. The solid arrows in the figure indicate the strong vertical transitions associated with interband structure in ϵ_2, such as the interconduction-band ($\pi^*\rightarrow\pi^*$) transitions, inter-valence-band–to-conduction-band transitions ($\pi\rightarrow\pi^*$) at the respective thresholds, and *M*-point $\pi\rightarrow\pi^*$ transitions. Weak transitions are indicated by the dashed vertical arrows. The curvature and average energy of each band are, respectively, directly related to the transfer integrals (γ's) and the site energy (δ's). The roles of these parameters in the determination of the shape and positions of the subbands can be understood from an intercomparison of the band-structure results for the stage-2, -3, and -4 compounds.

In the case of stage-2 KC_{24}, there are no interior carbon layers and the two bounding carbon layers are equivalent as required by the model symmetry. The band structure is determined only by the γ_i's, and not the δ_i's. The (k-dependent) splitting of the two conduction bands, and the splitting of the two valence bands, are both caused by the interlayer coupling via γ_1, γ_3, and γ_4. The nonzero values of γ_3 and γ_4 are responsible for the loss of mirror symmetry about the zero-energy ($E=0$) plane, as

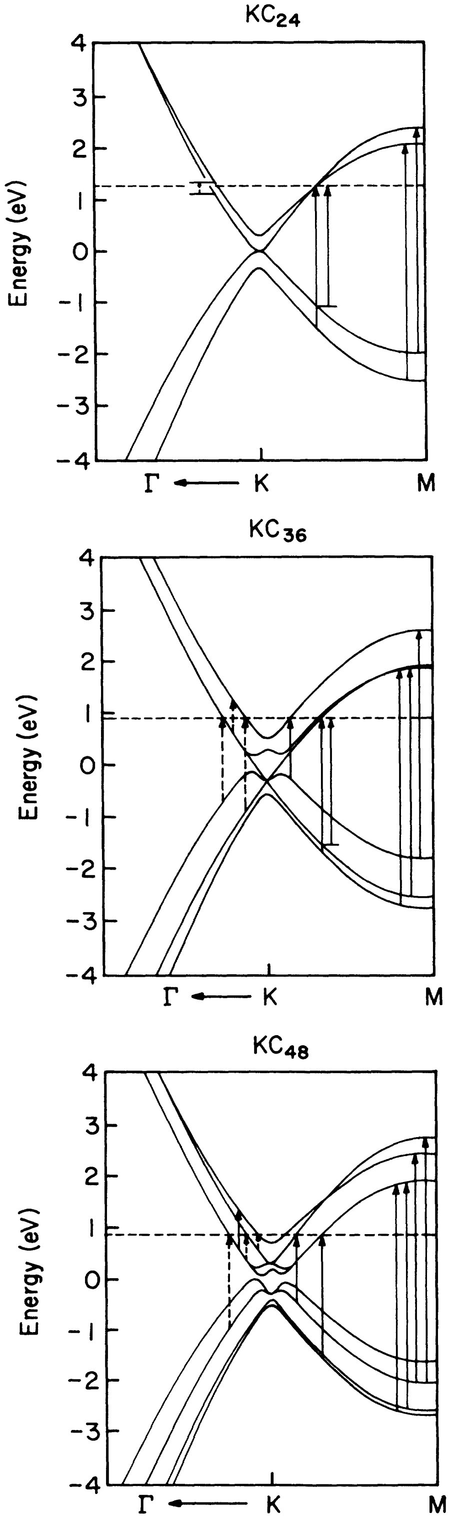

FIG. 5. Energy bands of stage-2–4 K GIC's along high-symmetry directions Γ-*K*-*M*. The Fermi level of each compound is designated by the dashed horizontal line. The solid and dashed arrows indicate, respectively, the principal intralayer and interlayer transitions.

well as the crossover of the two conduction bands near the Fermi level along the *K-M* direction. Saito and Kamimura[10] have pointed out that this band crossover will produce another path for electron travel through different carbon layers, consequently enhancing the orbital paramagnetism. It should be noted that the γ_3 and γ_4 parameters were set equal to zero in the 2D tight-binding model of Blinowski and Rigaux.[5,15]

For stage-3 KC_{36}, there are two equivalent bounding carbon layers and one interior carbon layer. The *c*-axis electrostatic potential associated with the differing net charge on interior and bounding layers is important, forcing one conduction band and one valence band further away from the plane of near mirror symmetry ($E=0$). The resulting relative shift between the energy bands amounts to a reduced interlayer coupling which is most noticeable near the *K* point. The up-shifted π and π^* bands are populated by electrons primarily localized in the interior graphite layers, while the remaining π and π^* bands are populated by electrons primarily localized in the bounding graphite layers. Therefore, we refer to these π bands below as "interior layer" or "bounding layer" bands.[28] The separation between these interior and bounding layer bands near E_F is approximately 2δ, which is the difference between the average electrostatic potential in the interior and bounding carbon layers.

The band structure of the stage-4 KC_{48} compound exhibits characteristics of both stage-2 and stage-3 K GIC's. As in the case of KC_{36}, the π^* energy bands associated primarily with electron density localized in the interior layers are up-shifted by 2δ with respect to those primarily associated with electrons localized in the bounding layers. In stage 4, the coupling between the bounding and interior layers is weaker than in stage 3 (i.e., the splitting of two lower conduction bands in stage 4 is less than that in stage 3). However, unlike the stage-3 compound, there are two adjacent interior layers with the same electrostatic potential. Therefore, the coupling between interior layers again becomes energetically favorable, and as a result, the two upper π^* bands and two upper π bands as separated in a way similar to that found for stage-2 KC_{24}.

The major differences between the present band structures and those of Saito and Kamimura[10] can be summarized as follows: (1) the present bands exhibit a smaller splitting between interior layer bands and bounding layer bands which is the result of our lower value for δ, and (2) the gap between the π and π^* bands near the *M* point(s) is much lower in the present work, and is a result of the *k* dependence we have introduced for γ_0. As a consequence of (1) and (2), the Fermi level and the $\pi^* \rightarrow \pi^*$ and $\pi \rightarrow \pi^*$ interband transition energies in the band structures of Saito and Kamimura[10] are all larger than in the present work.

Finally, it is worth noting the similarity of the π,π^* bands in Figs. 5(a)–5(c) to those of pristine graphite, except very close to the *K* point. For $E \cong E_F$, the dispersion is quite similar, and the splitting between the subbands is approximately described by a rigid relative displacement whose value reflects the *c*-axis distribution of net layer charge.

B. Dielectric function

In Fig. 6, we display the present results for the interband contribution to the dielectric function $\epsilon_2^{\text{inter}}(\omega)$, where $\epsilon_2^{\text{inter}} = \epsilon_2 - \epsilon_2^{\text{Drude}}$. The calculated results (solid line) and experimental data (+) for stage-2–4 K GIC's are shown along with the results we calculated according to the complete set of parameters of Saito and Kamimura[10] (dashed line). It is clear from the figure that the parameter changes we have made in the model Hamiltonians of Saito and Kamimura have improved significantly the agreement between theory and experiment.

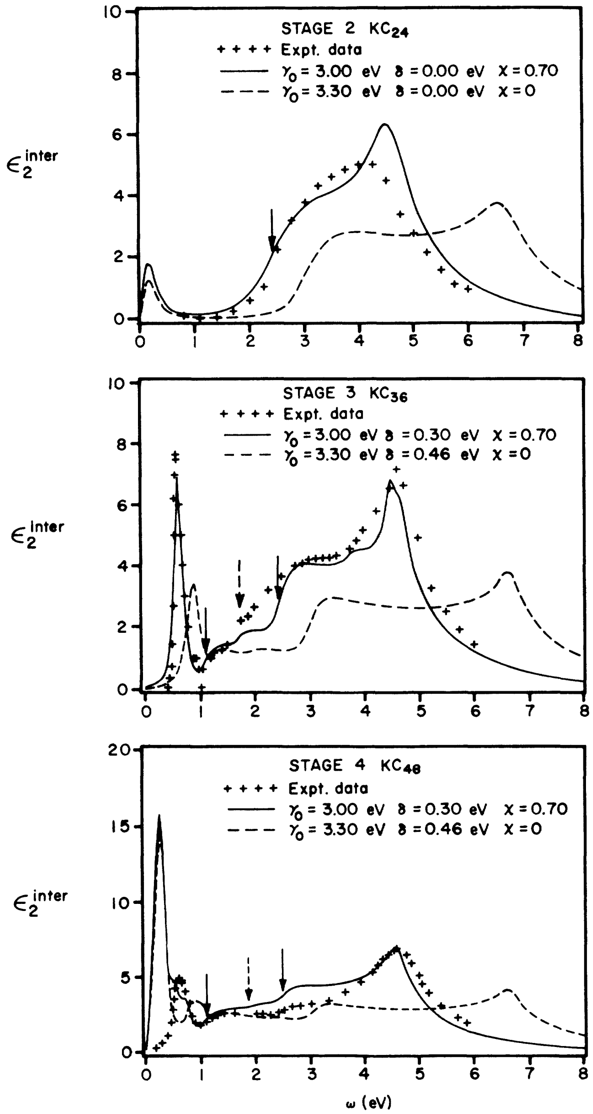

FIG. 6. Interband dielectric functions for stage-2–4 K GIC's. Indicated in the figure are the experimental data (+), the present calculations based on an extension of the model of Saito and Kamimura (Ref. 10) (solid line), and those calculated using the parameters and model of Ref. 10 (dashed line). The solid and dashed arrows indicate, respectively, our calculated values for the intralayer and interlayer $\pi \rightarrow \pi^*$ interband threshold energies.

The value for τ in Eq. (7) was primarily chosen to fit the width of the narrow $\pi^* \rightarrow \pi^*$ peaks at low energies and the width of the interband threshold ($\pi \rightarrow \pi^*$). On this basis, we find values of τ equal to 2×10^{-14}, 6×10^{-14}, and 4×10^{-14} s for the stage-2, -3, and -4 K GIC's, respectively, which can be compared to the value $\tau=2\times10^{-14}$ s obtained by Johnson and Dresselhaus[22] for pristine graphite. Thus, we find lifetimes in the donor-type GIC's equal to, or somewhat greater than, those in pristine graphite.

One may identify the structure in $\epsilon_2^{\text{inter}}(\omega)$ with characteristic band gaps and splittings in the stage-2–4 band structures shown in Figs. 5(a)–5(c). The calculated absorption peaks in $\epsilon_2(\omega)$ near 0.2 and 0.6 eV correspond to the vertical $\pi^* \rightarrow \pi^*$ transitions indicated in Figs. 5(a)–5(c). Peaks are obtained because the π^* bands involved are nearly parallel. There is noticeably much larger asymmetry in the 0.2-eV peak than in the 0.6-eV peak, reflecting the fact that the bands split by 0.6 eV exhibit the most similar dispersion. The calculated 0.2-eV peak is not observed in the data and is associated with transitions between π^* bands which are populated with electrons primary localized in adjacent graphite layers with the same electrostatic potential energy. The splitting between these bands is determined by the interlayer coupling parameters γ_1, γ_2, and γ_4. For KC_{36} and KC_{48}, the higher-energy peak in $\epsilon_2^{\text{inter}}(\omega)$ calculated near 0.6 eV is associated with transitions between interior and bounding layer π^* bands which are split by 2δ. *Thus, the 0.6-eV structure in the data is a direct measure of electrostatic potential energy difference between the bounding and interior graphite layers.* As shown in Fig. 6, the dashed curves calculated from the bands of Saito and Kamimura[10] exhibit this inter-conduction-band structure near 0.9 eV, reflecting their larger value for 2δ; furthermore, they predict M-point absorption at $\sim$6 eV rather than at 4.5 eV, which is observed experimentally.

We were unable to observe the broad low-energy 0.2-eV peak which is evident in the calculated dielectric function (Fig. 6) for KC_{24} and KC_{48} compounds. This is best shown in the $(1/\omega\epsilon_2)$-versus-ω^2 plots of Fig. 2, which allows one to most easily separate free-carrier and interband contributions to $\epsilon_2(\omega)$. Since our data are for $\hbar\omega > 0.2$ eV, we could only hope to separate the high-energy tail of the 0.2-eV peak from the much larger $1/\omega^3$ Drude background. In this regard, we note that free-electron background contributions to $\epsilon_2(\omega)$ at $\omega=0.2$ eV is 27 times larger than that at $\omega=0.6$ eV. Thus the 0.6-eV peak is much easier to observe experimentally.

In Fig. 6, the rise of $\epsilon_2^{\text{inter}}(\omega)$ at energies above $\sim$1 eV is due to the onset of valence-band–to-conduction-band ($\pi \rightarrow \pi^*$) absorption. The threshold involves transitions to π^* states at E_F. Shung[29] has shown that electron-electron scattering will broaden significantly the $\pi \rightarrow \pi^*$ interband thresholds. In the case of the stage-2 KC_{24} compound, the two principle thresholds are at 2.5 and 2.7 eV [Fig. 5(a)]. Even the calculated structure in $\epsilon^{\text{inter}}(\omega)$, in agreement with out data, does not resolve the individual $\pi \rightarrow \pi^*$ thresholds due to lifetime-broadening effects [τ in Eq. (7)]. A single, broad interband threshold is observed in stage 2 with a midpoint value $E_{\text{th}} \approx 2E_F + 0.1$ eV (solid arrow in Fig. 6). In the case of the stage-3 KC_{36} and stage-4 KC_{48} compounds, our theoretical results indicate that the strongest $\pi \rightarrow \pi^*$ thresholds arise from transitions between interior π and π^* bands, and between bounding π and π^* bands [Figs. 5(b) and 5(c)]. The separation between these π and π^* bands at the threshold is $\sim 2E_F + 2\delta$, and this energy should correspond to the midpoint of the inter-π-band threshold. Both of these thresholds are resolved in the calculated $\epsilon_2^{\text{inter}}(\omega)$ (Fig. 6) because they are well separated in energy; their positions and widths are in good agreement with experiment. It can be seen that the highest-energy, $\pi \rightarrow \pi^*$ threshold in stages 3 and 4 ($2E_F + 2\delta$) is most prominent in the data, consistent with our calculations. This results from the correspondingly higher joint density of states. The stage-3 and -4 $\pi \rightarrow \pi^*$ thresholds at $E_{\text{th}} \approx 2E_F$ are due to transitions between bounding and interior layer bands and these thresholds are indicated by dashed arrows in Fig. 6. The matrix elements for these $\pi \rightarrow \pi^*$ thresholds are also smaller than those involved in the thresholds at $2E_F \pm 2\delta$. Consequently, the corresponding jump in $\epsilon_2(\omega)$ at the dashed arrows is noticeably less, in agreement with the data. The calculated and experimental threshold energies are listed in Table III. We note, in general, that the experimental widths of the interband thresholds for KC_{36} and KC_{48} are somewhat broader than the calculated widths (Fig. 6). This agreement could be improved if a larger value for τ in Eq. (7) were used. Of course, the same value for τ cannot be expected to describe equally well both the broadening of the low-energy $\pi^* \rightarrow \pi^*$ and the high-energy $\pi \rightarrow \pi^*$ interband structures.

C. *c*-axis charge distribution

For stage index $n>2$, the net c-axis layer charge ρ_{net} self-consistently depends on the c-axis electrostatic potential and is sensitive to the value of δ in the present model. Our results for ρ_{net} differ noticeably from results obtained from the self-consistent band structure of Ohno and Kamimura[9] and the related results of Saito and Kamimura.[10] As we have discussed, our lower value of δ is necessary to explain the position of the sharp inter-conduction-band optical features in $\epsilon_2(\omega)$ for stages 3 and 4 at $2\delta \sim 0.60$ eV. Table IV compares our values for the net charge density in each graphite layer to those obtained from ^{13}C NMR studies by Kume, Nomura, and Hiroyama[30] and to the calculations of Ohno and Kamimura.[9] Layer charge densities were determined from the spin-lattice relaxation time T_1 obtained for the bounding and interior carbon layers. Applying the Korringa relation $N_j(E_F) \propto (T_1 T)^{-1/2}$, where $N_j(E_F)$ is the density of states of jth layer at the Fermi energy and T is the temperature, Kume and co-workers determined the fractional net charge f_j on the jth layer. Assuming linear π-band dispersion near E_F, i.e., $f_j^2 \propto N_j(E_F)$, they find $f_j \propto T_1 T$. For convenience, in comparing results, we define the fractional net charge η residing in the interior layer as $\eta = f_i/(f_i+f_b)$, where f_i and f_b are, respectively, the net charge residing in the interior and bounding layers. In the case of the stage-3 KC_{36} compound, the NMR and present work are in excellent agreement, with $\eta=9\%$,

TABLE III. Principal vertical inter-π-band transitions energies. The energies correspond to the optical transitions indicated by the vertical arrows in Fig. 5.

	Transition energy (eV)					
	Stage 2 ($E_F^{\rm calc}=1.28$ eV)		Stage 3 ($E_F^{\rm calc}=0.92$ eV)		Stage 4 ($E_F^{\rm calc}=0.88$ eV)	
Interband transition	Expt.	Calc.$^{\rm e}$	Expt.	Calc.$^{\rm e}$	Expt.	Calc.$^{\rm e}$
$\pi^*\rightarrow\pi^*$		0.15	$0.57^{\rm a}$	0.60		0.25
			$0.63^{\rm a}$		$0.60^{\rm a}$	0.55
					$0.73^{\rm a}$	0.70
$\pi\rightarrow\pi^*(E_F)^{\rm d}$	$2.5^{\rm b}$	2.5	$1.1^{\rm b}$	1.1	$1.1^{\rm b}$	1.1
		2.7	$1.7^{\rm b}$	1.7	$2.0^{\rm b}$	1.8
			$2.1^{\rm b}$	2.5	$2.5^{\rm b}$	2.5
$\pi\rightarrow\pi^*(M)^{\rm d}$	$4.5^{\rm c}$	4.4	$4.7^{\rm c}$	4.4	$4.7^{\rm c}$	4.5
		4.5		4.5		4.5
				4.7		4.6
						4.7

[a] From oscillator fits to ϵ_2 (see Table I).

[b] Obtained from the midpoint of the threshold in the $\epsilon_2(\omega)$ data.

[c] Obtained from the position of the peak in the $\epsilon_2(\omega)$ data.

[d] Only the principal $\pi\rightarrow\pi^*$ transitions are listed.

[e] Obtained from the position of structure in $\epsilon_2^{\rm calc}(\omega)$ in the limit $\tau\rightarrow\infty$.

while the theoretical value of η obtained by Ohno and Kamimura[9] is 1.3%, about an order of magnitude smaller. Unfortunately, there are no NMR results for η for the stage-4 KC_{48} compound. We calculate $\eta=16\%$ for stage-4 KC_{48}, which is larger than our value $\eta=9\%$ obtained for stage-3 KC_{36}, and less than the value $\eta=18\%$ obtained from NMR data[30] for stage-6 KC_{60}. Ohno and Kamimura[9] reported a value of $\eta=2.6\%$ for stage-4 KC_{48}, which is much less than the values obtained from the present work or that obtained from the NMR data.

It is interesting to consider the excess electron density of each subband in the higher-stage compounds (Table V). We find fractional charge densities of 8% and 15.4% for the upper π^* bands of KC_{36} and KC_{48}, respectively, and these values are very close to the values we calculate for the fractional charge density in the interior layers, 9% for KC_{36} and 16% for KC_{48}. This result demonstrates that the upper and lower π^* bands are, indeed, primarily associated with the interior and bounding carbon layers, respectively, and the mixing between layer wave functions is weak.[28]

TABLE IV. Experimental and calculated fractional layer charge for the interior (i) and bounding (b) carbon layers for stage-2–6 K GIC's.

Stage	Layer	NMR$^{\rm a}$ (%)	This work (%)	Ohno *et al.*$^{\rm b}$ (%)
2	b	50	50	50
3	b	45	45.5	49.3
	i	10	9.0	1.3
4	b		42	48.5
	i		8.0	1.3
6	b	41		48.5
	i_1	6.0		1.2
	i_2	3.0		0.3

[a] Reference 30.

[b] Reference 9.

D. Fermi-surface properties

Figure 7 shows our results for the extremal basal-plane orbits for the stage-2–4 K GIC's. They are centered at the six K point(s), one of which is shown in the figure. Since all the conduction bands are partially filled, the number of orbits is equal to the number of the conduction (π^*) bands. Consistent with the band structures shown in Figs. 5(a)–5(c), the orbits with the smallest average radii correspond to the highest-energy conduction bands. For stage 4, orbits associated with the nearly degenerate pair of lower-lying conduction bands cannot be distinguished on the scale of the figure.

The orbit area $S(E_F)$ was calculated according to

$$S(E_F)=\tfrac{1}{2}\int_0^{2\pi}\kappa_F^2(\phi)d\phi\ , \tag{10}$$

where $\kappa_F(\phi)$ is the length of the Fermi wave vector in a particular subband measured relative to the K point, and ϕ is the polar angle. Table V compares our calculated areas with those obtained from de Haas–van Alphen (dHvA) data by Higuchi, Suematsu, and Tanuma[31] and Dresselhaus, Leung, and Chieu.[32] Although a few orbit areas for KC_{36} and KC_{48} match well with experimental observations, we find that the overall agreement between theory and the dHvA experiments is not very good. For example, large orbits with predicted areas of

TABLE V. The extremal Fermi-surface cross-sectional areas and fractional electron density associated with each subband of stage-2–4 K GIC's.

	Experimental		This calculation	
Stage	Observed dHvA frequency (T)	Extremal cross-sectional area ($\text{cm}^{-2}\times 10^{14}$)		Excess electron density of subband (%)
2^a	133	1.26	13.35	43
	149	1.42	17.35	57
	282	2.69		
	306	2.92		
	306	2.92		
3^b	146	1.40	2.44	8
	260	2.50	13.6	45
			14.0	47
4^b	121	1.16	1.00	3.4
	144	1.38	3.5	12
	238	2.28	12.5	42
	264	2.53	12.6	43
	338	3.24		

[a]Experimental data, Dresselhaus, Leung, and Chieu (Ref. 32).
[b]Experimental data, Higuchi, Suematsu, and Tanuma (Ref. 31).

$(12-17)\times 10^{14}$ cm^{-2} for stage-2–4 K GIC's have not been observed experimentally. A possible explanation might involve scattering at Brillouin-zone boundaries arising from large in-plane superlattices. However, for the two common superlattices such as $(\sqrt{7}\times\sqrt{7})R\,19°$) (Ref. 33) or $(\sqrt{12}\times\sqrt{12})R\,30°$) (Ref. 17) previously proposed in these compounds, we find that the largest orbits still fit inside the reduced-area zones formed by the appropriate zone folding of the hexagonal 2D zone of Fig. 3. The absence of reported high-frequency dHvA orbits for stage-2–4 K GIC's needs to be addressed in future work. It may simply be due to experimental difficulties in the K GIC's. Good agreement between optical[34] and Fermi-surface studies[35] of the (acceptor) SbCl$_5$ GIC's has been obtained, however.

In Fig. 8, we plot the density of states at the Fermi energy $D(E_F)$ versus reciprocal stage index $1/n$ for various alkali-metal GIC's. The results are from the present work (∗), Ohno (●), and specific-heat data of Mizutani, Kondow, and Suganuma[36] (△,□), and Suganuma, Kondow, and Mizutani[37] (○). The experimental data exhibit a weak dependence on the particular alkali-metal atom. This behavior is consistent with the picture that the band structure near the Fermi surface of stage-2–4 K GIC's is

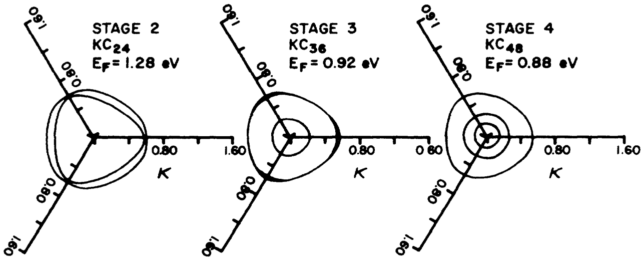

FIG. 7. Extremal orbits calculated according to the present work for stage-2–4 K GIC's. The three axes join at a K point in the Brillouin zone and connect to the three closest M points. The wave vectors are plotted in units of $1/a$, where $a=2.46$ Å is the in-plane unit-cell lattice vector.

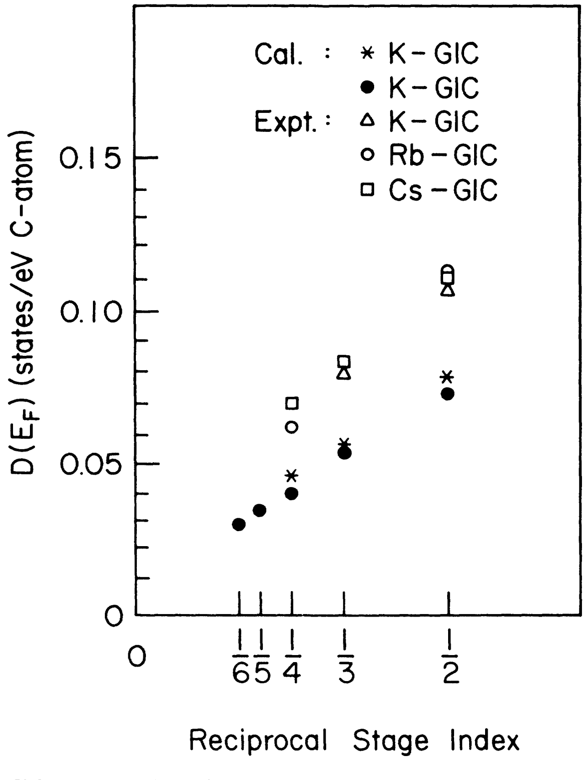

FIG. 8. Density of states $D(E_F)$ at the Fermi level vs reciprocal stage index $1/n$ for alkali-metal GIC's.

primarily determined by the spacing between adjacent carbon layers (~ 3.35 Å), the net electron density in the carbon layers, and not the thickness of the intercalate layer. The primary roles of the alkali-metal layers can then be viewed as donating electrons to the π^* graphitic bands and decoupling the system along the c axis. As seen from Fig. 8, our calculated values for $D(E_F)$ are larger than those of Ohno and Kamimura,[9] but still considerably smaller than experimental values. The electron-phonon interaction is probably responsible for this discrepancy.

Introducing the electron-phonon enhancement, the density of states at E_F is then given by

$$D^*(E_F)=(1+\lambda)D(E_F) , \qquad (11)$$

where $D^*(E_F)$ is the enhanced DOS, λ is the dimensionless electron-phonon coupling constant, and $D(E_F)$ is the bare electronic DOS calculated in the absence of electron-phonon coupling. Estimating λ by comparing our value of $D(E_F)$ to specific-heat data,[36,37] we find $\lambda=0.3$, 0.4, and 0.49, respectively, for stage-2, -3, and -4, K GIC's. A value of 0.35, irrespective of stage index, has been calculated by Inoshita and Kamimura[38] using a metallic sandwich model in which *all* the excess electrons reside in the bounding carbon layers. Our estimates for λ are in reasonable agreement with Inoshita and Kamimura for the stage-2 and -3 compounds. For the stage-4 compound our estimate is considerably higher. However, it must be kept in mind that the optical and NMR results indicate that the excess electron density in the interior graphite layers of high-stage K GIC's is far from the value of zero used by Inoshita and Kamimura in their calculation. Assuming the specific-heat data are correct, the experimental results suggest that excess electrons in the interior layers contribute in a significant way to the average electron-phonon coupling constant λ.

VI. SUMMARY

To quantitatively understand the optical data of the stage-2–4 donor-type GIC's we have calculated the dielectric function using the tight-binding 2D model of Saito and Kamimura.[10] Some of the band parameters were adjusted to bring the calculated interband dielectric functions into agreement with our optical data. Most important, the value of the electrostatic potential parameter δ was lowered, and a k dependence of γ_0 (in-plane transfer integral) was introduced. Comparing the calculated dielectric function to the experimental data, we were able to obtain good quantitative agreement between the experimental and calculated dielectric functions for all three stages. Various important vertical interband transitions have been identified with characteristic band splittings. We have shown that the position of a prominent inter-π^*-band peak in ϵ_2 at 0.6 eV for $n \geq 3$ is approximately equal to 2δ, where δ is the key band parameter controlling the distribution of excess electron density between interior and bounding carbon layers. The c-axis charge distribution calculated from our model is in excellent agreement with that determined from ^{13}C NMR measurements of Kume and co-workers.[30] From the present work, the net fractional charge in the interior carbon layers is found to be 9% and 16% for stages 3 and 4, respectively. Our values for the calculated density of states at E_F for stage-2–4 K GIC's are smaller than values obtained from specific-heat measurements,[36,37] but the discrepancy can be attributed to electron-phonon coupling which enhances $D(E_F)$ by a factor of 1.3–1.5, depending on stage index. We also have calculated the stage-dependent extremal electron-orbit areas, and find there is noteworthy disagreement with those obtained from de Haas–van Alphen experiments[31,32] indicating further Fermi-surface studies may still be needed.

ACKNOWLEDGMENTS

The authors are grateful to Dr. A. W. Moore of Union Carbide for his generous gift of HOPG used in this study. We would like to acknowledge Professor M. S. Dresselhaus, Dr. G. Dresselhaus, Professor H. Kamimura, and Dr. R. Saito for helpful discussions. The research at University of Kentucky was supported by the U.S. Department of Energy under Grant No. DE-FG05-85ER45151 and the University of Kentucky Research Foundation.

---

[1] For a review of GIC's, see M. S. Dresselhaus and G. Dresselhaus, Adv. Phys. **30**, 139 (1981); S. A. Solin, Adv. Chem. Phys. **49**, 455 (1982).

[2] Recent conference proceedings are also published in *Intercalation in Layered Materials*, edited by M. S. Dresselhaus (Plenum, New York, 1987).

[3] L. Pietronero, S. Strassler, H. R. Zeller, and M. J. Rice, Phys. Rev. Lett. **41**, 763 (1978).

[4] S. A. Safran and D. R. Haman, Phys. Rev. B **32**, 606 (1980).

[5] J. Blinowski and C. Rigaux, J. Phys. (Paris) **41**, 667 (1980).

[6] P. Hawrylak, Ph.D. thesis, University of Kentucky, 1985 (unpublished).

[7] S. Y. Leung and G. Dresselhaus, Phys. Rev. B **24**, 3490 (1981).

[8] S. Shimamura and A. Morita, J. Phys. Soc. Jpn. **51**, 502 (1982).

[9] T. Ohno and H. Kamimura, J. Phys. Soc. Jpn. **52**, 223 (1983).

[10] R. Saito and H. Kamimura, Synth. Met. **12**, 295 (1985); R. Saito, Ph.D. thesis, University of Tokyo, 1984 (unpublished).

[11] C. Rigaux, in *Intercalation in Layered Materials,* Ref. 2, p. 235.

[12] P. C. Eklund, M. H. Yang, and G. L. Doll, in *Intercalation in Layered Materials,* Ref. 2, p. 257.

[13] N. Chen and S. Rabii, Phys. Rev. B **31**, 4784 (1985).

[14] D. M. Hoffman, P. C. Eklund, R. E. Heinz, P. Hawrylak, and K. R. Subbaswamy, Phys. Rev. B **31**, 3973 (1985).

[15] J. Blinowski, N. H. Hau, C. Rigaux, J. P. Vieren, R. LeToullec, G. Furdin, A. Herold, and J. Melin, J. Phys. (Paris) **41**, 47 (1980).

[16] D. E. Nixon and G. S. Parry, J. Phys. D **1**, 291 (1968).

[17] W. Rudoff and H. Schulz, Z. Anorg. Allg. Chem. **238**, 156 (1954).

[18] S. A. Solin, Physica **99B**, 443 (1980).

[19] D. M. Hoffman, H. R. Heinz, G. L. Doll, and P. C. Eklund, Phys. Rev. B **32**, 1278 (1985).

[20] J. Zhang, D. M. Hoffman, and P. C. Eklund, Phys. Rev. B **34**, 4316 (1986).

[21] C. C. Sheih, R. L. Schmidt, and J. E. Fischer, Phys. Rev. B **20**, 3351 (1979).

[22] L. G. Johnson and G. Dresselhaus, Phys. Rev. B **7**, 2275 (1973).

[23] F. Wooten, *Optical Properties of Solids* (Academic, New York, 1972), p. 248.

[24] $\gamma_i = \langle \phi_{2p_z}(\mathbf{r}) \,|\, H(\mathbf{k}) \,|\, \phi_{2p_z}(\mathbf{r} - \mathbf{R}_{i_\alpha}) \rangle$. The $\mathbf{R}_{i_\alpha}$ connect the appropriate C atoms (see Fig. 4). The self-energy integral is given by $U_{j_\alpha} = \langle \phi_{2p_z}(\mathbf{r} - \mathbf{R}_{j_\alpha}) \,|\, H(\mathbf{k}) \,|\, \phi_{2p_z}(\mathbf{r} - \mathbf{R}_{j_\alpha}) \rangle$. There are four inequivalent carbon sites in the stage-3 and -4 K GIC's. The Hamiltonian parameters (δ, δ_j) can be written as linear combinations of the U_{j_α} (see Ref. 10).

[25] Our conclusions are not sensitive to the details of the functional form chosen for $\gamma_0(\kappa)$. The function must simply exhibit a gradual decrease from the value 3.0 eV at the *K* point to 2.3 eV at the *M* point. For example, the functions $f_1(\kappa) = 3$ eV $[1 + C_1(\kappa/\kappa')]^{-1}$ [Eq. (4)], $f_2(\kappa) = 3$ eV $[1 - C_2(\kappa/\kappa')]$, and $f_3(\kappa) = 3$ eV $[1 - C_3(\kappa/\kappa')^2]^{1/2}$ all yield similar results for $\epsilon_2(\omega)$ provided that the C_j are chosen to yield $\gamma_0(\kappa) = 2.3$ eV at the *M* point. The interband contribution to $\epsilon_2(\omega)$ below 6 eV is dominated by thresholds for $\pi \rightarrow \pi^*$ absorption near the *K* point (1–2.5 eV) and absorption near the *M* point (3–5 eV).

tion near the *M* point (3–5 eV).

[26] J. M. Ziman, *Principles of the Theory of Solids* (Cambridge University Press, Cambridge, England, 1972), p. 135.

[27] See Ref. 26, pp. 137.

[28] $\psi_k = \sum_i a_{k,\imath} \phi_{k,i}^{\text{layer}}$, where ψ_k are eignfunctions of the Hamiltonian $H(k)$, and the $\phi_{k,i}^{\text{layer}}$ are Bloch wave functions built from orbitals centered in the *i*th carbon layer. The interlayer coupling parameters $(\gamma_1, \gamma_3, \gamma_4)$ will mix different-layer Bloch wave functions to form eigenfunctions of the Hamiltonian. Our results and those of Saito and Kamimura (Ref. 10) indicate that the mixing is small.

[29] K.W.-K. Shung, Phys. Rev. B **34**, 1264 (1986).

[30] K. Kume, K. Nomura, and Y. Hioryama, Synth. Met. **12**, 307 (1985).

[31] K. Higuchi, H. Suematsu, and S. Tanuma, J. Phys Soc. Jpn. **48**, 1532 (1980).

[32] G. Dresselhaus, S. Y. Leung, and T. C. Chieu, Synth. Met. **2**, 321 (1980).

[33] N. Kambe, G. Dresselhaus, and M. S. Dresselhaus, Phys. Rev. B **31**, 3491 (1978).

[34] D. M. Hoffman, R. E. Heinz, R. E. Heinz, G. L. Doll, and P. C. Eklund, Phys. Rev. B **32**, 1278 (1985).

[35] H. Zaleski, P. K. Ummat, and W. R. Datars, J. Phys. C **17**, 3167 (1984).

[36] U. Mizutani, T. Kondow, and M. Suganuma, Phys. Rev. B **17**, 3165 (1978).

[37] M. Suganuma, T. Kondow, and U. Mizutani, Phys. Rev. B **23**, 706 (1981).

[38] T. Inoshita and H. Kamimura, Synth. Met. **3**, 223 (1981).